Interfacial characteristics between bitumen and corrosion products on steel slag surface from molecular scale

Haiqin Xu [a,b], Yingxue Zou [a], Gordon Airey [b], Haopeng Wang [c], Hanyu Zhang [b], Shaopeng Wu [a,*], Anqi Chen [a,*], Jun Xie [a], Yang Liang [d]

[a]   State Key Laboratory of Silicate Materials for Architectures, Wuhan University of Technology, Wuhan 430070, China;

[b]   Nottingham Transportation Engineering Centre, Faculty of Engineering, University of Nottingham, University Park, Nottingham NG7 2RD, UK;

[c]   Department of Civil and Environmental Engineering, University of Liverpool, Liverpool, L69 3BX, UK

[d]   Highway Bureau, Ministry of Transport,   China

* Correspondence author: wusp@whut.edu.cn (S. Wu), anqi.chen@whut.edu.cn (A. Chen).

ABSTRACT

Corrosion commonly happened on the surface of steel slag during the weathering and accumulation process, whose products would form weak points and affect the interface between bitumen and steel slag. To clear its characteristics in the atomic scales, the interface between bitumen and corrosion products was investigated by molecular dynamics (MD) simulations. Firstly, bitumen model, corrosion products model and bitumen-corrosion products systems were constructed. Different simulated temperatures were applied on the systems to reach equilibrium with NVT (constant number of atoms, volume, and temperature) ensemble. The interaction effect in the interface were evaluated by geometric adsorption index, interaction energy, adhesion work and surface free energy. Diffusion coefficient and relative concentration were used to evaluate the diffusion and aggregation. Finally, the pull-out test was conducted on the equilibrium models to determine the debonding behaviors at the interface. The results show that the interaction effect in Bitumen-FeO system was the strongest while that in Bitumen-FeOOH system was the weakest, which can be proved by surface free energy and debonding behaviors. The temperature changing would affect van der Waals energy but had no obvious association with coulombic energy. The adhesion between bitumen and corrosion products was contributed by non-bond interaction energy which consisted of van der Waals interaction for Fe_3O_4, Fe_2O_3 and FeOOH, and van der Waals and electrostatic interaction for FeO. The most severe aggregation of bitumen occurred in Bitumen-FeO system, which was more likely caused by electrostatic interaction. Furthermore, the change of velocity

34 and thickness led to the failure transformation from cohesion to adhesion. The strong

35 interaction in Bitumen-FeO system increase the possibility of cohesion failure in the debonding

36 process.

37

38 Key words: Adhesion, Steel slag, Corrosion product, Asphalt mixture, Molecular dynamic

39

40 1 Introduction

41   Asphalt concrete have been widely applied in the pavement engineering widely for its

42 outstanding service characteristics including comfort driving, low noise, superior skid

43 resistance, simplicity of maintenance [1]. In Europe, more than 90% of roads are constructed

44 with asphalt concrete, supporting 80% of passenger transportation and 70% of inland cargo

45 transportation [2,3]. Also, there are over 1.2 million kilometers of asphalt concrete pavement in

46 China that sustains the whole transportation system [4]. Along with the globalization of trade

47 and economic, more road tasks including construction and maintenance are being needed to

48 undertake the transportation flow. However, the tasks would significantly consume lots of

49 resources, especially the natural aggregate which accounts for 95% of the asphalt concrete in

50 weight. The consumption will cause severe damages to the environment eventually. Therefore,

51 the development of harmless, green and sustainable materials for pavement engineering has

52 become the emergency.

53   In the recent years, recycling solid wastes into pavement engineering have been widely

54 accepted as an effective approach to reduce exploitation of natural resources and eliminate

55 pollution to environment [5,6]. Steel slag, the classical solid waste produced during the

56 steelmaking process, have been proved its feasibility of application as aggregate in asphalt

57 concrete. The previous studies have proved the success of recycling steel slag as coarse and fine

58 aggregates, and reusing steel slag powders as the fillers in asphalt concrete of different

59 gradations, micro-surfacing, chip seals and thin friction course [7–10]. Commonly, the excellent

60 service performances of steel slag asphalt concrete are contributed by the pores structure and

61 the high alkalinity to strength the steel slag-bitumen interface [11–13]. Shen et al. have

62 investigated the mechanism of adhesion property between steel slag and rubber modified

63 asphalt and proved its better adhesion property than the natural aggregate like diabase [14].

64 Cui et al. have applied active adhesion evaluation method (AAEM) on the adhesion evaluation

65 of aggregate and bitumen, and also enlarged superior adhesion characteristic of steel slag

66 compared to basalt [15]. Liu et al. have claimed that the adhesion performance between the

67 bitumen and steel slag were improved by chemical reactions due to amine and amide N–H

68 stretching vibrations and SiOH stretching vibrations [16]. Furthermore, different investigations

69 of the interface interaction between steel slag and bitumen have been also reported. Guo et al.

70 have evaluated the long-term water stability of asphalt mixtures containing steel slag aggregate,

71 and the results show that proper addition of steel slag would enhance the water stability but

72 the steel slag could hydrate and produce microcracks on the surface, which would finally result

73 in the failure of the interface [17]. Coomarasamy and Walzak found that the debonding of the

74 interface between steel slag aggregate and asphalt mastic in asphalt pavement happened

75 randomly, and the formation of calcium carbonate ($CaCO_3$)-rich deposits at the surface of some

76 SSA particles in moist condition caused cracks [18]. It was inferred that some SSA particles have

77 free calcium oxide (f-CaO) at the surface, which is the main cause for the $CaCO_3$-rich deposits,

78 because f-CaO can be transformed into $CaCO_3$ by reacting with water and carbon dioxide (CO_2)

79 in moist condition. Therefore, the random destruction of the interface between steel slag and

80 bitumen still presents challenges to researchers.

81   In fact, the formation and accumulation of iron mineral are also the reasons and important

82 beginning of adhesion failure apart from hydration of steel slag. Though some research has

83 claimed that the possibility of the rust formation of steel slag aggregate is low; in fact, it is

84 closely related to the composition of steel slag caused by the production process [19]. Steel slag

85 is complex mixture that mainly consists of the elements of Ca, Fe, Si, and O, and the nonmetallic

86 oxides such as C_3S and C_2S are the main components in steel slag [20]. However, it can be found

87 that there are still some iron simple substance and iron oxide existing in the steel slag, especially

88 the steel slag processed by imperfect treatment processes in developing countries [21]. Iron

89 simple substance is considered as the residual product after steelmaking, magnetic separation,

90 and crush process due to the difference in the production technique. The formation and existing

91 form of iron oxide are more complicated, and the possible source is steel slag's long-term

92 outdoor complex aging. Figure 1 shows the aged steel slag sample obtained from Hunan Valin

93 Steel Co., Ltd. It can be found that there is enough elemental iron in the steel slag, so that it can

94   be attracted by the magnet. Meanwhile, rust is attached on the surface of steel slag obviously.

95   The iron materials will be reacted with the environment easily during the weathering and

96   accumulation treatment. The reaction would result in severe corrosion and generate the

97   corrosion products in crystal form. The corrosion products would be changed according to the

98   different environment, for example that the corrosion products consist of the crystal substances

99   like magnetite, goethite, lepidocrocite when iron materials are exposed to saline-alkali

100   environment [22,23]. The inner layer of corrosion products was composed of magnetite, while

101   the outer layer of which was mainly composed of goethite and lepidolite [24]. In the process of

102   mixing, the interface between these corrosion products and bitumen is not close enough, and

103   the weak bonding cause weak interface and stress concentration easily, which makes it more

104   easily being destroyed. Furthermore, the occurrence and growth of the corrosion products

105   would replace the position of steel slag in the original interface, which would also damage the

106   strong interface interaction between bitumen and steel slag possibly. However, there are few

107   investigations on the interface of corrosion products and bitumen, Therefore, it is necessary to

108   investigate the interface between bitumen and corrosion products on steel slag.

109
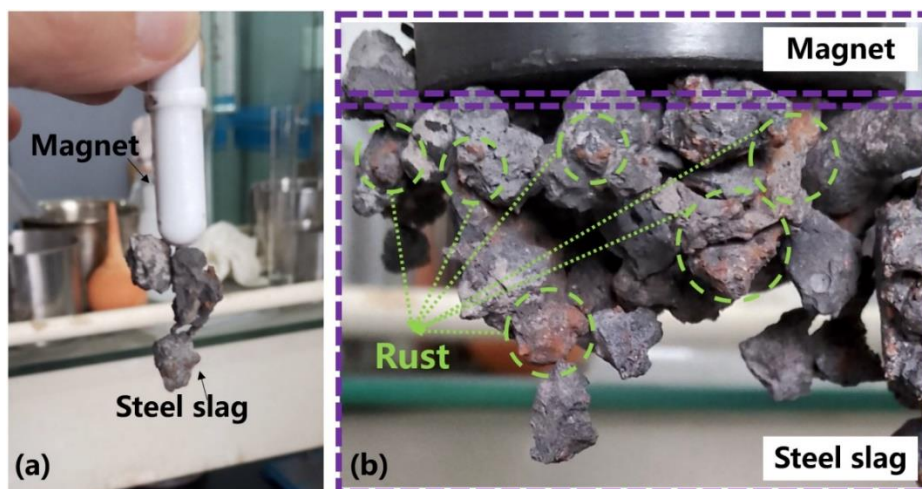
Figure 1 Steel slag sample from Hunan Valin Steel Co., Ltd after weathering: (a) Steel slag
attracted by magnet; (b) Corrosion products on the steel slag surface

113

114   Molecular Dynamics (MD) simulation is the method that is suitable for the adhesion failure

115   caused by the movements and dislocation of nanoparticles. The MD method is a well-

116   established tool for investigating atomic motions at the molecular scale [25]. It describes the

117   motions and positions of atoms based on Newton's second law. During the simulation,

118   empirical force-field equations are used to describe interatomic forces, electron interactions,

119   and other energies. The MD method can describe various scales and indicators, such as the

120   change in energy of the proton system, mean-square displacement of the atomic system, and

121   adsorption state between atoms [26,27]. These indicators are physical quantities that have been

122   demonstrated to be describable by MD, both theoretically and experimentally [28–30]. In

123   contrast to the phenomenological method usually applied for deformation, spalling, and

124   cracking, it isn't restricted by experimental methods and specimen preparation conditions and

125   can effectively reduce the shortcomings of macroscopic scales [31]. Several studies conducted

126   by MD simulation have been carried out to investigate the interaction between bitumen and

127   crystal substances. Gao et al have evaluated the adhesion properties and debonding behaviors

128   of bitumen-mineral interface systems of four representative minerals (quartz, calcite, albite and

129   microcline) with and without water [32]. Huang et al studied the diffusion law of bitumen on

130   the surface of two typical minerals of aggregate (SiO_2 and CaO) and interfacial behaviour at

131   microscale [33]. Guo et al, Gao et al and Zhao et al have investigated the interfacial adhesion

132   behavior between mineral crystal and SBS modified asphalt, rubber asphalt, epoxy resin

133   emulsified asphalt and polyurethane-modified asphalt respectively [34–37]. Sun et al analyzed

134   the interfacial interaction mechanism between three bitumen of different SARA components

135   content and metal oxides crystal (CaO, MgO, Al_2O_3 and Fe_2O_3) [38]. The previous research have

136   proved the successful application of MD method in the adhesion investigation between

137   bitumen and crystal substances. Moreover, there are also a few molecular dynamics studies on

138   the adhesion interface between steel slag and bitumen. Liu et al conducted tricalcium silicate

139   (C_3S) as the main component as steel slag to simulate the distribution and adhesion of asphalt

140   components on steel slag [39]. Zhou et al chosen $(SiO_2)_2$ with ICSD No. 81097 as the steel slag

141   to investigate surface and interface adhesive properties between steel slag and bitumen [40]. It

142   can be found that the current research mainly focused on the interaction between bitumen and

143   major mineral crystal, a few work has investigated that of bitumen and steel slag, and there is

144   almost no research about the adhesion and debonding of the bitumen-corrosion products

145   interface at the molecular scale. As a result, there is necessity for understanding the interface

146   characteristics of bitumen-corrosion products at the molecular scale, which would be

147   investigated in the study.

148   The main purpose of this research is to investigate the interfacial characteristics between

149   bitumen and corrosion products by MD simulations. The bitumen model and corrosion

150   products of Fe_2O_3, Fe_3O_4, FeO and FeOOH were built firstly. Then bitumen-corrosion products

151   systems were constructed, and different simulated temperatures were applied to reach

152   equilibrium. The interaction in bitumen-corrosion products systems was evaluated by

153   geometric indexes, interaction energy, adhesion work and surface free energy. Diffusion and

154   aggregation of bitumen on the surface of corrosion products were analyzed by diffusion

155   coefficient and relative concentration. Finally, the pull-out test was conducted to investigate

156   the debonding process.

157

158   2 Molecular dynamic simulation

159   *2.1 Model establishment*

160   Bitumen is a by-product of the crude oil refining process, which is produced by separating

161   lighter fractions from heavy crude oil. It results that bitumen is the typical hydrocarbon mixture

162   made up of a variety of functional groups and atoms such as oxygen, nitrogen, and sulfur.

163   Based on the different molecular sizes and solubility, the bitumen can be classified into four

164   components (asphaltene, saturate, aromatic, and resin) that can be represented by one or more

165   molecules to form the molecular model for bitumen. The AAA-1 bitumen model proposed by

166   Li and Greenfield has 12 components (as shown in Figure 2) and its rheological and mechanical

167   properties were proved closer to experimental data compared with previous models [41].

168   Therefore, the AAA-1 bitumen model was determined to be used in this research. Figure 2

169   lists the parameters of represented components in detail.

170   Materials studio software was used for the model establishment and thermodynamic

171   properties calculation. 12-components molecules models for bitumen were built in 3D

172   Atomistic. Condensed-phase optimized molecular potentials for atomistic simulation studies

173   (COMPASS) was selected as the force field, which can predict and calculate the structure and

174   thermophysical properties of common inorganic and organic system over a large temperature

175   and pressure range [42]. The model was constructed with the following step: Firstly, the model

176   was constructed by Amorphous Cell tools with an initial density of 0.1 g/cm^3 under the three-

177 dimensional cycle condition. The geometric optimization with 5000 iterations was followed to

178 eliminate unreasonable configurations in the model, leveling off the energy of the molecule to

179 reach minimum energy. Then, Forcite tools was used to reach dynamic equilibrium for the

180 stable structure and density, where a canonical ensemble (NVT, constant molecule number,

181 model volume, and temperature) with 298 K, 1 fs time step for 100 ps and an isothermal-

182 isobaric ensemble (NPT, constant atomic number, pressure, and temperature) with 298 K and

183 1.0 atm were conducted successively. The temperature and pressure of the block were

184 controlled by Andersen barostat and Nose-Hoover-Langevin thermostat. Moreover, the Ewald

185 with the accuracy of 0.001 kcal/mol and Atom-based with the cutoff distance of 15.5 Å are

186 assigned as the Electrostatic and van der Waals summation method. Finally, the models have

187 been established for further performance prediction and analysis in terms of thermodynamics

188 parameters, structural characteristics, and dynamic behaviors. The rationality and reality of

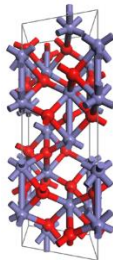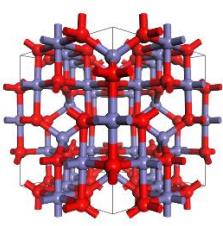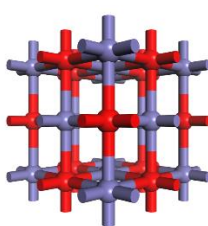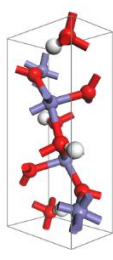189 this model have been proved in our previous studies [31].

190
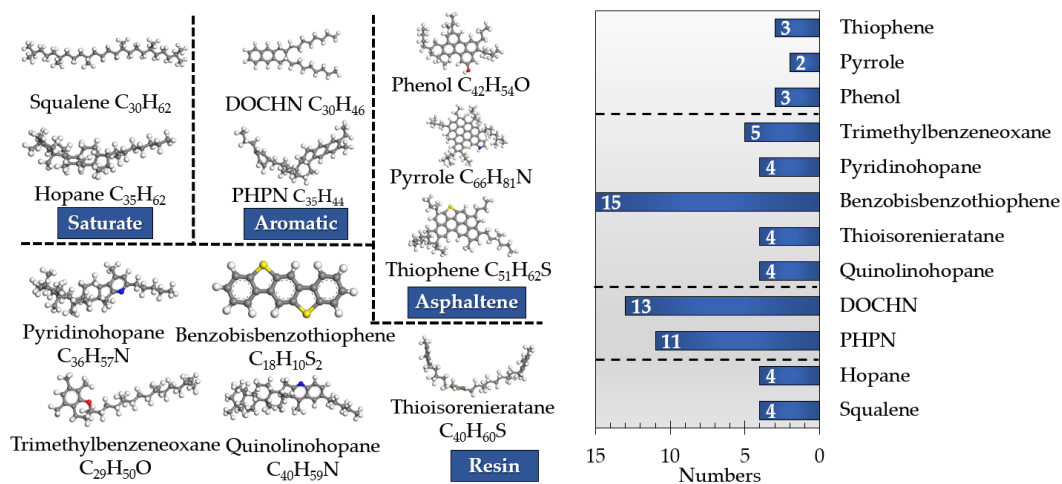
191
192 Figure 2. 12-components molecules models for bitumen and the components numbers

193

194 Commonly, the corrosion products are mainly composed of Fe_2O_3, Fe_3O_4, FeO and FeOOH

195 [43,44]. In this research, different corrosion products, rather than isomers of the same products,

196 are the focus, therefore α-Fe_2O_3 (Hematite), Fe_3O_4 (Magnetite), FeO and α-FeOOH (Geothite)

197 were firstly selected as the corrosion products. The unit cell constants and unit cell structure

198 models of Fe_2O_3, Fe_3O_4, FeO and FeOOH used in this study were shown in Table 1 [45–48]. The

199 lattice structure of α-Fe_2O_3 is hexagonal close packing. The cell contains two Fe^{3+} ions and three

200 O^{2-} ions. Each Fe^{3+} ion is surrounded by eight O^{2-} ions and four adjacent Fe^{3+} ions. Each O^{2-} ion

201 is surrounded by two Fe^{3+} ions. Fe^{3+} ions form triangular layers and O^{2-} ions fill the gaps of

202 these layers. The crystal structure of Fe_3O_4 is face-centered cubic system, and there are eight

203 iron ions and sixteen O^{2-} ions in the structure cell. In the crystal structure of FeO, the

204 arrangement of iron ions and oxygen ions is very orderly. Each iron ion is surrounded by six

205 oxygen ions, and each oxygen ion is also surrounded by six iron ions. α-FeOOH is an

206 orthogonal crystal system, and the unit cell of α-FeOOH contains four FeOOH, in which the

207 anions in the structure of α-FeOOH are arranged in hexagonal close packing, and each Fe^{3+} and

208 its surrounding anions form $FeO_3(OH)_3$ octahedron.

209

210 Table 1. Unit cell of corrosion products and lattice parameters

Corrosion Products	Fe_2O_3	Fe_3O_4	FeO	FeOOH
Unit cell structure				
Unit cell constants	a = 5.035 Å b = 5.035 Å, c = 13.720 Å; $\alpha=\beta$ = 90 °, γ=120 °	a = 8.394 Å b = 8.394 Å c= 8.394 Å; $\alpha=\beta=\gamma$=90 °	a = 4.332 Å b = 4.332 Å c= 4.332 Å; $\alpha=\beta=\gamma$=90 °	a = 4.604 Å, b = 9.951 Å, c = 3.019 Å; $\alpha=\beta=\gamma$=90 °

211

212 The supercell models of corrosion products were also established by Materials studio

213 software and the steps were as follows: Firstly, an orthorhombic lattice was converted into an

214 orthorhombic lattice. The plane's crystal face was sliced using the Cleave Surface tool with

215 specific Miller index where (1 0 0) was for Fe_3O_4, FeO, (1 1 0) was for Fe_2O_3 and (0 1 0) was for

216 FeOOH. The reason for the adoption of crystallographic surface plane was that these

217 crystallographic surfaces showed the least lattice mismatch shown in the previous research that

218 adsorption and diffusion of organic molecules happened on iron oxide surfaces, meanwhile

219 the oxygen ions were full bulk-coordination on the surfaces [49–51]. Then, before performing

220 energy reduction on the unit cell structure, it was necessary to ensure that the COMPASS force

221 field of each atom in the corrosion products unit cell was accurately assigned and that chemical

222   linkages between atoms were deleted. Finally, the optimized unit cell model was enlarged to a

223   supercell model and a certain vacuum layer was added. The establishment of the supercell

224   model of Fe$_2$O$_3$ molecule was as an example shown in Figure 3 (a), and the supercell models of

225   corrosion products and their parameters were shown in Figure 3 (b). The interface model has

226   three layers: a corrosion products layer as the foundation, a bitumen layer on top of the

227   corrosion products layer, and a 50 Å vacuum layer on top of the bitumen layer. Figure 3 (c)

228   shows four interface models.

229
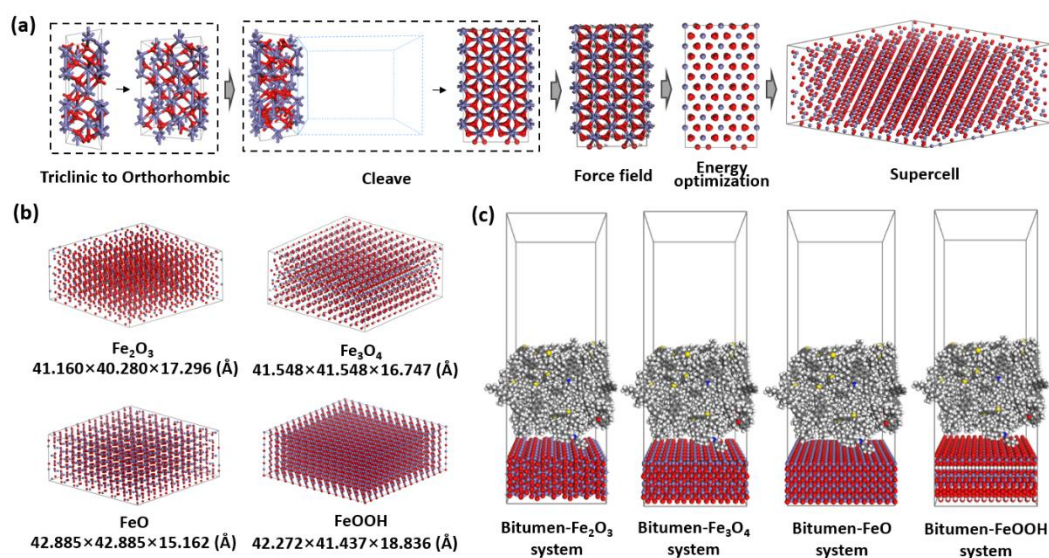
230

231   Figure 3. The establishment of models: (a) Supercell model of Fe$_2$O$_3$; (b) Supercell model of
232   corrosion products; (c) Bitumen-corrosion products interface models

233

234   *2.2 Simulation conditions*

235   In this study, a classical molecular dynamics code: the large-scale atomic/molecular

236   massively parallel simulator (LAMMPS) was used to perform the simulation. The polymer

237   consistent force field (PCFF) was chosen for bitumen simulation, which has been validated to

238   describe the organic, inorganic, and organic–inorganic interface systems. The force field is an

239   empirical expression of the potential energy surface, and the total energy of the molecules is

240   the sum of kinetic energy and potential energy. Moreover, the total potential energy is

241   composed of bond angle bending potential energy, bond stretching potential energy, dihedral

242   angle twisting potential energy, off-plane vibration potential energy, van der Waals potential

243   energy and Coulomb electrostatic potential energy, shown in Equations (1).

$$E_{\text{potential}} = \sum_{\text{cross}} E(b, \theta, \varphi) + \sum_{\text{bond}} E_b(b) + \sum_{\text{torsion}} E_\varphi(\varphi)$$
$$+ \sum_{\text{angle}} E_\theta(\theta) + \sum_{\text{inversion}} E_x(x) + E_{ele} + E_{vdw} \qquad (1)$$

244　where $E_{\text{potential}}$ is the total energy; $\sum_{\text{cross}} E(b, \theta, \varphi)$ represents the cross term potential

245　energy; $\sum_{\text{bond}} E_b(b)$ is the bond stretching potential energy; $\sum_{\text{torsion}} E_\varphi(\varphi)$ is the dihedral

246　angle twisting potential energy; $\sum_{\text{angle}} E_\theta(\theta)$ is the bond angle potential energy;

247　$\sum_{\text{inversion}} E_x(x)$ is the off-plane vibration potential energy; E_{ele} is the Coulomb electrostatic

248　potential energy and E_{vdw} is the van der Waals potential energy. The interaction between

249　bitumen and corrosion products can be described by the 6/9 Lennard–Jones potential, as shown

250　in Equations (2)-(3). The LJ 9-6 and Coulombic interactions are truncated to 10 Å and 8 Å.

$$E_{\text{ele}} = \sum_{i>j} \frac{q_i q_j}{r_{ij}} \qquad (2)$$

$$E_{vdw} = \sum \varepsilon_{ij} \left[2 \left(\frac{r_{ij}^0}{r_{ij}} \right)^9 - 3 \left(\frac{r_{ij}^0}{r_{ij}} \right)^6 \right] \qquad (3)$$

251　where q_i and q_j are the charges of atomic i and j; r_{ij} is the distance of atomic i and j

252　and ε_{ij} is the well depth of atomic i and j, respectively.

253　　　Each simulation of the interface model consists primarily of the following steps: (1) Energy

254　minimization was used firstly to remove potential energy excess that existed in the initial

255　configuration. (2) The bitumen-corrosion products system was then relaxed using NVT

256　(constant number of atoms, volume, and temperature) ensemble at the different simulated

257　temperature 293 K, 313 K, 333 K, 353 K and 373 K for 1 ns to reach the equilibrium state.

258　Simultaneously, the corrosion products layer in each model was fixed and each valence state

259　of iron atom was arranged to the corrosion products for the whole simulation process to

260　precisely calculate the indicators of bitumen-corrosion products system. Then the final

261　bitumen-corrosion products system after 373 K simulation were chosen for the investigation of

262　debonding behaviors, which are shown in Figure 4 (a). In the debonding process, the top

263　bitumen would be fixed to control the thickness of bitumen film, and the basement of the

264　corrosion products would move to conduct the debonding, meanwhile the temperature was

265　determined as 293 K and the whole process was under NVT ensemble. Its schematic diagram

266　of loading mode is shown in the Figure 4 (b) and its loading parameters are shown in the Figure

267　4 (c). As shown in the Figure 4 (d), the adhesion during the debonding process can be evaluated

268   by area according to the Equation (4):

$$CR = \frac{Area\,1}{Area\,2} \times 100\% \tag{4}$$

269   Where CR was the cohesion rate, $Area\,1$ was the area of the basement of the corrosion

270   products and $Area\,2$ was the area of the bitumen still attached on the surface of corrosion

271   products after debonding.
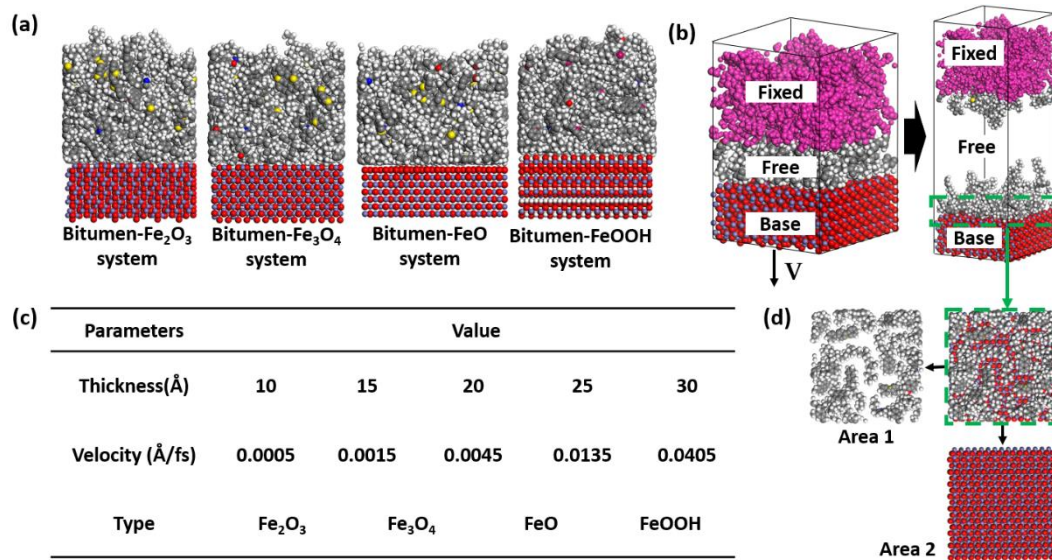
273   Figure 4. Characterization of debonding behaviors between bitumen and corrosion products:
274   (a) The model for debonding test; (b) Loading mode; (c) Loading parameters; (d) Adhesion
275   evaluation

276

277   *2.3 Adhesion and diffusion evaluation indexes*

278   2.3.1 Relative concentration distribution

279   To obtain insight into the aggregation configuration of bitumen on various corrosion

280   product surfaces, the relative concentration was computed as the ratio of the atom number in

281   the unit volume perpendicular to the axis to the atom number in the unit volume of the

282   amorphous unit. The three-dimensional periodic system should be partitioned into evenly

283   spaced plates in the interfacial system. The distribution of atomic density in each plate was

284   then computed to give the overall structure's relative concentration distribution.

285   2.3.2 Interaction energy and adhesion work

286   Interaction energy (E_{inter}) could be used to evaluate the stability of interface of bitumen

287   and corrosion products. Adhesion work ($W_{adhesion}$) could be used to stand for the interfacial

288   bonding strength of bitumen and corrosion products. The greater the absolute value of E_{inter}

289 and W_{adhesion}, the more interaction there was between bitumen and corrosion products. When

290 the value of E_{inter} was zero or positive, adsorption was minor or non-existent. Their

291 calculation formula was shown in Equation (5) and (6).

$$E_{inter} = E_{pe-bitumen} + E_{pe-corrosion\,products} - E_{pe-total} \tag{5}$$

$$W_{adhesion} = \frac{E_{inter}}{A} \tag{6}$$

292 Where E_{inter} represented the interaction energy between bitumen and corrosion products,

293 $W_{adhesion}$ represented the adhesion work between bitumen and corrosion products, $E_{pe-total}$

294 represented that the total potential energy of the bitumen-corrosion products system in a

295 steady state, $E_{pe-bitumen}$ represented the total potential energy of bitumen,

296 $E_{pe-corrosion\,products}$ represented the total potential energy of corrosion products and A

297 represented the contact area of bitumen and corrosion products, considered as the size of

298 supercell model.

299 2.3.3 Mean square displacement and diffusion coefficient

300   The core regulation of diffusion phenomena was the movements of atoms in three-

301 dimension space, which was vital to analyze the interaction between bitumen and corrosion

302 products. However, due to the enormous number of atoms in the interface system, detecting

303 each atom's motion trajectory is difficult. As a result, mathematical statistics method was held

304 to describe the regularity of particle movement. The most used indicator was mean square

305 displacement (MSD), which would be represented and calculated by Equation (7):

$$MSD(t) = (|r_i(t) - r_i(0)|^2) \tag{7}$$

306 Where, $MSD(t)$ indicated as the mean value of all atoms' movement positions in the molecular

307 system, $r_i(0)$ indicated the original position of particle i, and $r_i(t)$ indicated the position of

308 particle i at the time of t.

309   Diffusion coefficient, for the measurement of the molecule's capacity for diffusion, rate at

310 which a quantity diffuses per unit area while the concentration gradient is the same unit.

311 MSD had a linear relationship with time and was correlated with the diffusion coefficient after

312 diffusion relaxation process. After this period, the linear slope of the MSD curve might be used

313 to compute the diffusion coefficient of the contact system, as indicated by Equation (8):

$$D = \frac{1}{6N} \lim_{t \to \infty} \frac{d}{dt} \sum_{i=1}^{N} (|r_i(t) - r_i(0)|^2) \tag{8}$$

314 Where, the diffusion coefficient was recorded as D in the interface system, N indicated the

315 whole number of molecules in the interface system, and the differential term was equal to the

316 linear slope of the interface system's MSD curve.

317   Equation (8) showed that there was a linear relationship between the diffusion coefficient

318 and the slope of the MSD curve. Nevertheless, Equation (8) ignored the actual simulation

319 scenario and was expressed in an ideal condition of indefinite period. As a result, Equation (9)

320 illustrates how the diffusion coefficient calculation formula was really approximated in the

321 calculation:

$$D \approx \frac{1}{6} K_{MSD} \tag{9}$$

322 Where K_{MSD} was equal to the linear slope of the interface system's MSD curve.

323

324 2.3.4 Contact angle test

325   The contact angle test was used to validate the adhesion interaction of corrosion products

326 at macroscale, which can be calculated by the surface free energy (SFE). It represents the ability

327 of a solid surface to interact with other objects, and the lager value means the stronger

328 interaction. The corrosion products were the analytical reagent provided by Shanghai Macklin

329 Biochemical Co., Ltd and Guangdong Wengjiang Chemical Reagents Co., Ltd. The CAs were

330 measured by the sessile drop method with Dataphysics OCA20, DataPhysics Instruments

331 GmbH, Germany. The CAs of corrosion products were measured by the probe liquids,

332 including distilled water, formamide and glycol. The final value was the average of three tests

333 for each group of samples. The SFE could be calculated by the Equation(10)-(11) [52,53]:

$$\gamma_L = \gamma_L^d + \gamma_L^P \tag{10}$$

$$\frac{\gamma_L(1 + \cos\theta)}{2} \frac{1}{\sqrt{\gamma_L^d}} = \sqrt{\gamma_s^P} \sqrt{\frac{\gamma_L^P}{\gamma_L^d}} + \sqrt{\gamma_s^d} \tag{11}$$

334 Where γ_L and γ_s represent SFEs of the corrosion products and the probe liquids, γ_L^d and γ_L^P

335 represent dispersive component and polarity component of the SFE of the probe liquids [54],

336 γ_s^d and γ_s^P represent dispersive component and polarity component of the SFE of the
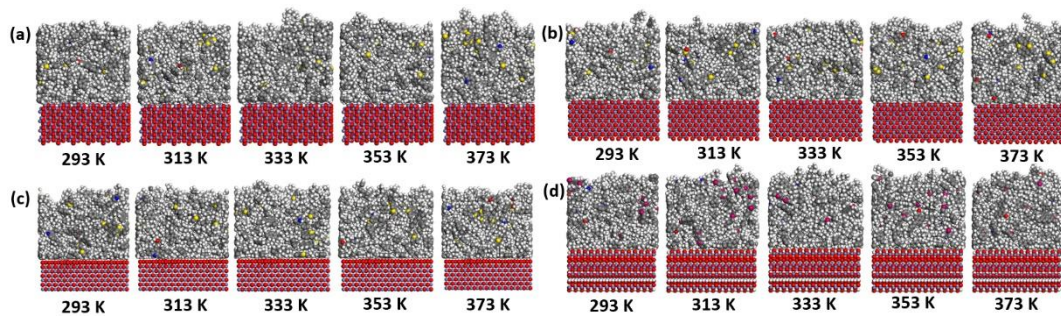
337   corrosion products.

338

339   3 Results and discussion

340   *3.1 Dynamic geometry changes of bitumen-corrosion products system*

341   The trajectory output files of bitumen-corrosion products systems were obtained to

342   observe the dynamic simulation. Figure 5 shows the simulation results of bitumen on the

343   corrosion products surface at different temperature for 1 ns. It can be found that bitumen

344   molecules would migrate to corrosion products spontaneously, and eventually diffuse and

345   absorb on the surface of corrosion products. Compared with Fe_2O_3, Fe_3O_4 and FeOOH, bitumen

346   would combine with FeO more closely. Moreover, little difference was found between each

347   bitumen-corrosion products systems at different temperature. The effect of temperature on the

348   degree of adsorption cannot be observed directly. It can be also observed that the bitumen

349   molecular cannot diffuse into the molecular vacancy on the surface of corrosion products,

350   which indicated that bitumen was hard to penetrate the corrosion products at the setting

351   simulated temperature, and diffusion and adsorption were the main migration form happened

352   in the systems.

353

355   Figure 5. The simulation results of bitumen-corrosion products systems: (a) Bitumen-Fe_2O_3;
356   (b) Bitumen-Fe_3O_4; (c) Bitumen-FeO; (d) Bitumen-FeOOH

357

358   To quantify the structure changing, the changing of size of simulation cell in Z direction

359   was selected and it was calculated by Equation (9):

$$\Delta l_z = \frac{l_{z-1ns}-l_{z-0ns}}{l_{bitumen}} \% \tag{9}$$

360   where l_{z-1ns} was the size of simulation cell in Z direction at 1 ns, l_{z-0ns} was the size of

361   simulation cell in Z direction at 0 ns, Δl_z represents the changing of size of simulation cell in

362   Z direction and $l_{bitumen}$ represents the size of bitumen originally in Z direction.

363   The larger Δl_z value means the closer adsorption between bitumen and corrosion

364   products. Structure changing of simulation cell in Z direction of bitumen-corrosion products

365   systems at different temperature was shown in Figure 6. It can be observed that the Δl_z value

366   of Bitumen-FeO system and Bitumen-Fe$_2$O$_3$ system would be reduced with fluctuation with the

367   temperature increased while that of Bitumen-FeOOH system and Bitumen-Fe$_3$O$_4$ system

368   increased first and then decrease dynamically. The results indicate that temperature increasing

369   cause atoms to move faster and interaction between atoms intensify, resulting in larger gaps

370   between atoms. This also shows that the adsorption between bitumen and corrosion products

371   was no longer tight in high temperature environments.

372
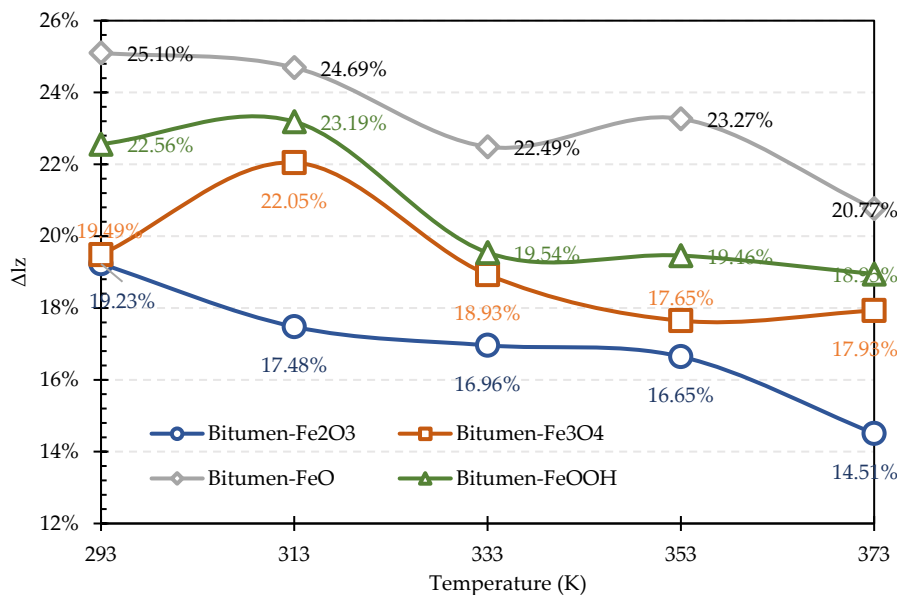
373
374   Figure 6. Z coordinate changes of simulation cell of bitumen-corrosion products systems at
375   different temperature
376

377   *3.2 Energy changes in bitumen-corrosion products systems*

378   Figure 7 shows the energy composition changes of bitumen-corrosion products systems at

379   different temperature, where TOTAL was referred as the total energy of the system, PE was

380   referred as the potential energy of the system, and KE was referred as the kinetic energy of the

381   system. The total energy of the systems would be converged after 200 ps. The values of PE, KE

382   and TOTAL were calculated as average of the energy in stable statement (600 ps to 1000 ps) of

383   the systems. It is clearly that the total energy of the systems was all increased when simulated

384   temperature was raised. It was supported by the increment of potential energy and kinetic

385   energy individually. This is mostly because the heat energy in the system is constantly

386   transformed into internal energy as the temperature rises, increasing the internal energy. The

387   kinetic energy of the systems was similar and would be increased gradually by the increased

388   temperature, which was related to the intensified irregular movements of molecules in bitumen.

389   The potential energy of Bitumen-Fe_2O_3 system, Bitumen-Fe_3O_4 system and Bitumen-FeOOH

390   system were similar while that of Bitumen-FeO system was obviously less. The potential energy

391   of Bitumen-Fe_2O_3 system and Bitumen-Fe_3O_4 system would be increased rapidly at 293 K and

392   313 K, then slowly at 333 K to 373 K. The potential energy of Bitumen-FeO system would be

393   increased gradually from 293 K to 353 K and sharply at 373 K, while the potential energy of

394   Bitumen-FeOOH system would be increased gradually with the temperature increasing.

395
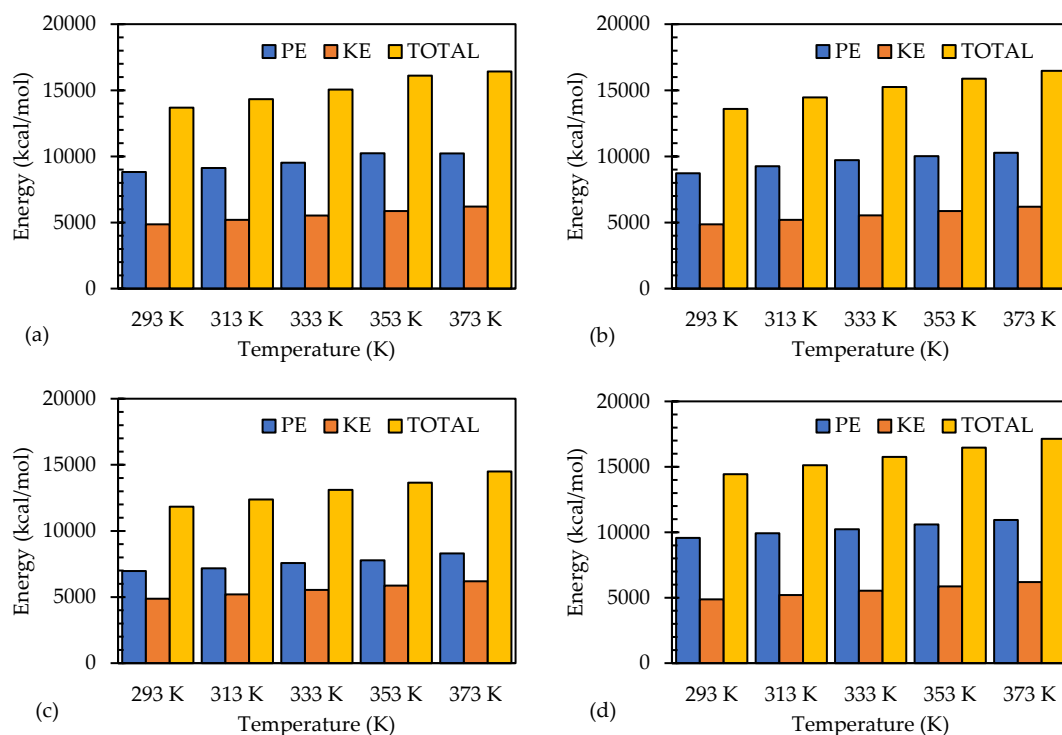
396   Figure 7. The total energy components of bitumen-corrosion products systems at different
397   temperature: (a) Bitumen-Fe_2O_3, (b) Bitumen-Fe_3O_4, (c) Bitumen-FeO, and (d) Bitumen-
398   FeOOH

399

400   The potential energy should be referred as the sum of bonding energy (E_{mol}) and non-

401   bonding energy ($E_{nonbonding}$). The non-bonding energy includes coulombic energy (E_{coul}) and van

402   der Waals energy (E_{van}). The non-bonding energy consists of cross term energy, bond stretching

energy, dihedral angle twisting energy, bond angle energy and off-plane vibration energy. Table 2 shows the changes of potential energy composition of bitumen-corrosion products systems at different temperatures. It can be found that the increment of temperature would result in decreasing the absolute value of van der Waals energy and increasing bonding energy of bitumen-corrosion products in a fluctuating way. Moreover, the variation law of coulombic energy had little correlation with the changes of simulated temperature. Van der Waals energy was found obviously less in Bitumen-FeOOH system and larger in Bitumen-FeO system, while that of Bitumen-Fe$_2$O$_3$ system and Bitumen-Fe$_3$O$_4$ system were similar. It indicates that intermolecular interaction in Bitumen-FeO system was stronger, and combination was more closely.

Table 2. The potential energy components of bitumen-corrosion products systems at different temperatures

		293 K	313 K	333 K	353 K	373 K
Bitumen-Fe$_2$O$_3$	E$_{van}$	-3021.49	-2970.65	-2917.20	-2886.73	-2833.55
	E$_{coul}$	44.85	-8.61	-18.16	366.86	-34.49
	E$_{mol}$	11800.48	12101.98	12462.70	12754.94	13091.18
Bitumen-Fe$_3$O$_4$	E$_{van}$	-3054.63	-3075.52	-2987.73	-2885.96	-2915.62
	E$_{coul}$	-32.45	208.20	241.69	141.56	92.57
	E$_{mol}$	11808.99	12123.93	12465.80	12757.03	13099.80
Bitumen-FeO	E$_{van}$	-5001.47	-4944.27	-4935.13	-4848.44	-4827.19
	E$_{coul}$	78.53	-52.79	27.91	-174.32	-8.17
	E$_{mol}$	11887.21	12174.07	12476.07	12805.94	13136.69
Bitumen-FeOOH	E$_{van}$	-2642.46	-2582.98	-2545.95	-2482.37	-2421.46
	E$_{coul}$	440.36	404.58	344.25	330.15	292.75
	E$_{mol}$	11771.84	12097.51	12431.12	12752.83	13069.18

* The unit of numerical value in the table is kal/mol

3.3 Interaction energy in bitumen-corrosion products systems

Table 3 shows interaction energy and its components that contributes to the adhesion between bitumen and corrosion products at different temperature, which was calculated based on Equation (1) and (4). It can be found that the E$_{inter}$ value equals to E$_{nonbonding}$ value, which indicates that the adhesion between bitumen and corrosion products was completely contributed by the non-bond interaction. The covalent interaction contributes little or nothing to the adhesion of bitumen-corrosion products systems, showing that no chemical bond is

formed between corrosion products and bitumen. It can be observed that in the Bitumen-Fe_2O_3 system, Bitumen-Fe_3O_4 system and Bitumen-FeO system, van der Waals was the mainly interaction effect between bitumen and corrosion products and the coulomb electrostatic contributed slightly. In the Bitumen-FeOOH system, the coulomb electrostatic interaction was significantly more strongly, though it was still weaker than the van der Waals interaction effect. This might be caused by the existence of hydroxyl in FeOOH, having an obvious electrostatic interaction with other materials, especially the bitumen showing acidity. It can be also found that E_{van} fluctuated slightly with temperature than E_{coul}, especially the coulombic energy of Bitumen-FeO system. With the temperature increasing, the activity of the atoms in Bitumen-FeO system would change rapidly, influencing the coulombic energy. The reason that temperature had little effect on van der Waals energy was that it was mainly related to the molecule mass and distance, which wouldn't be affected by temperature. In brief, the adhesion between bitumen and corrosion products was attributed by nonbonding interaction energy. Van der Waals interaction was the major contribution in Bitumen-Fe_2O_3 system, Bitumen-Fe_3O_4 system and Bitumen-FeO system, meanwhile it wasn't affected obviously by temperature. The adhesion in Bitumen-FeOOH system was contributed by both van der Waals interaction and electrostatic interaction, while it would decease when temperature was raised up.

Table 3 Interaction energy components of bitumen-corrosion products systems at different temperature

		293 K	313 K	333 K	353 K	373 K
Bitumen-Fe_2O_3	E_{inter}	-1183.01	-1241.07	-1251.45	-868.48	-1279.84
	E_{van}	-1210.51	-1225.47	-1216.48	-1212.93	-1240.17
	E_{coul}	27.50	-15.60	-34.98	344.45	-39.67
	$E_{nonbonding}$	-1183.01	-1241.07	-1251.45	-868.48	-1279.84
Bitumen-Fe_3O_4	E_{inter}	-1311.83	-1146.00	-1068.15	-1118.28	-1254.01
	E_{van}	-1277.74	-1341.73	-1279.90	-1244.79	-1330.82
	E_{coul}	-34.09	195.74	211.75	126.51	76.81
	$E_{nonbonding}$	-1311.83	-1146.00	-1068.15	-1118.28	-1254.01
Bitumen-FeO	E_{inter}	-3190.99	-3342.17	-3272.40	-3464.46	-3293.34
	E_{van}	-3251.84	-3271.15	-3285.94	-3266.16	-3267.11
	E_{coul}	60.85	-71.02	13.54	-198.30	-26.23
	$E_{nonbonding}$	-3190.99	-3342.17	-3272.40	-3464.46	-3293.34
Bitumen-FeOOH	E_{inter}	-389.01	-439.04	-479.89	-478.56	-504.44
	E_{van}	-816.83	-815.58	-817.30	-802.33	-802.15
	E_{coul}	427.82	376.54	337.40	323.77	297.71

	$E_{nonbonding}$	-389.01	-439.04	-479.89	-478.56	-504.44

445 * The unit of numerical value in the table is kal/mol

446

447   The adhesion work of bitumen-corrosion products systems at different temperature are

448 shown in Figure 8. It can be observed that the adhesion work of bitumen and corrosion

449 products at different temperatures fluctuates without obvious regularity with the increment of

450 simulated temperature, the results of which was similar to the previous research about the

451 adhesion between bitumen and aggregate [35,55]. For a certain corrosion products type and

452 temperature, $W_{adhersion}$ of Bitumen-FeO system was much higher than that of other systems,

453 which indicates that FeO had more powerful adhesion ability to bitumen. $W_{adhersion}$ of Bitumen-

454 Fe_2O_3 system and Bitumen-Fe_3O_4 system was similar to each other and that of Bitumen-FeOOH

455 system was the minimum. As van der Waals interaction accounted for the most contribution of

456 the adhesion energy in the systems, the differences would mainly result from the distribution

457 of the atoms in the cell structure and the distance between corrosion products and bitumen.

458 Consistent with the previous studies, Rath et al. have investigated oleate adsorption on iron

459 oxides including (hematite, magnetite, and goethite), and the results show that oleate binds

460 strongest on magnetite followed by hematite and goethite, which are consistent with the

461 weakest interaction of FeOOH in this study [50]. Furthermore, Iveson et al. have focused on

462 contact angle measurements of iron ore powders, and the results indicated that the higher the

463 goethite content or the less the magnetite content , the smaller the contact angle, which also

464 shows the weak interaction effect of goethite [56]. In view of these phenomenon, it is possible

465 to consider controlling the rusting stage by regulating the storage environment, storage

466 atmosphere and storage time in the yard, and thus to obtain the desired rusting products. For

467 instance, increasing the amount of FeO can result in a thicker bitumen film, which can control

468 the failure pattern at the interface. Figure 4 represents the CA and SFE of corrosion products

469 obtained from contact angle test. It can be found that the SFE value of FeO was the largest while

470 that of FeOOH was the smallest, and that of Fe_2O_3 and Fe_3O_4 were similar. The results indicate

471 that FeO had the strongest interaction effect with the other objects. This trend is consistent with

472 the simulated results, which also shows the same order of the interaction effect.

473
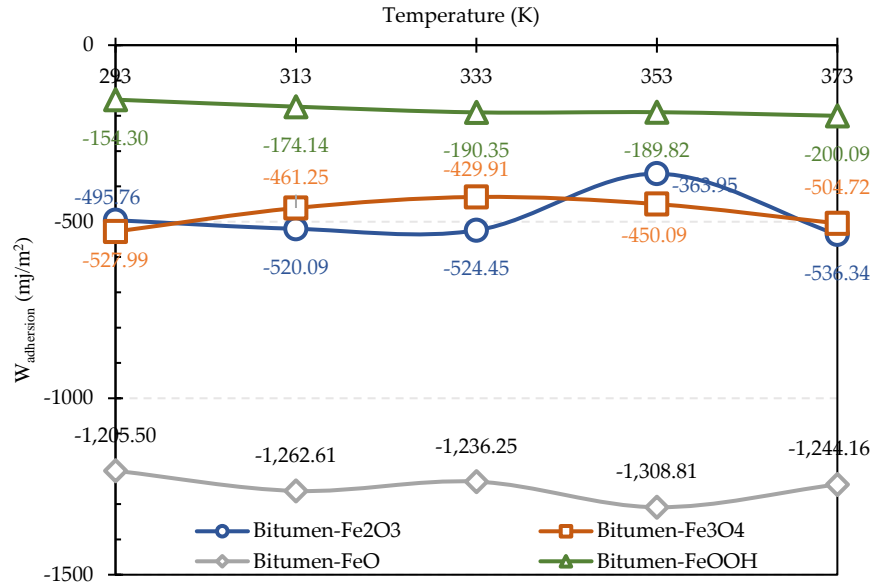
Figure 8. $W_{adhesion}$ of bitumen-corrosion products systems at different temperature

Table 4. CA and SFE of corrosion products

| | CA (degree) | | | SFE (mJ/m²) | | |
	Water	Glycol	Formamide	γ	γ^p	γ^d
Fe_2O_3	8.9	40.0	20.8	79.7	77.8	1.9
Fe_3O_4	10.4	40.0	23.0	79.8	78.0	1.8
FeO	11.0	46.5	27.5	84.3	82.9	1.4
FeOOH	17.3	46.1	20.3	76.6	74.8	1.9

3.4 Diffusion behavior of bitumen-corrosion products systems

Mean squared displacement (MSD) is used to investigate the molecules movement of bitumen on the corrosion products over simulated time. The MSD curves of bitumen-corrosion products system at different temperatures are shown in Figure 9. It can be found that the MSD curves can be divided into two stages (rapid rising period and linear rising period). The rapid rising period would last for a short time and then linear rising period was followed which can be used to calculate the diffusion coefficient. The MSD calculation was based on simple diffusion mode (Brownian motion), during which MSD was a quadratic function of correlation time in the initial short time, representing barrier-free directional diffusion. With the increase of correlation time, MSD will quickly transform to a linear function stage, which represents normal diffusion. This linear function region is generally the best region for calculating diffusion coefficient. Especially in Bitumen-FeO system, it can be found that rapid rising

491   period in Bitumen-FeO system almost show as a vertical upward line, which was obviously

492   short. It might be caused by the strong van der Waals interaction between bitumen and FeO.

493   Then the MSD curves of Bitumen-FeO system are the lowest ones, indicating that the diffusions

494   are inhibited, and the adsorption degrees are higher currently. It was in accordance with the

495   analysis results of the interaction energy.

496   The movement of bitumen in systems would be increased by the higher temperature,

497   except Bitumen-FeO system, indicating that higher temperature would be beneficial to the

498   mobility of the bitumen molecules. It can be explained by the aggregation degree of bitumen

499   on the corrosion products which would be discussed in section 3.5. As for the Bitumen-FeO

500   system, there wasn't obvious law between the MSD and temperature in this system. It can be

501   also observed that the MSD of Bitumen-FeO system was larger at 293 K and 313 K, and that of

502   Bitumen-Fe_2O_3 system and Bitumen-Fe_3O_4 system were larger at 333 K, 353 K and 373 K. It

503   would be related to the stability of the corrosion products: compared with Fe_2O_3 and Fe_3O_4,

504   FeO would be more unstable with the temperature increasing and expose the activity which

505   might reduce the MSD through contact and interaction.

506

(a) Bitumen-Fe_2O_3 (b) Bitumen-Fe_3O_4

(c) Bitumen-FeO   (d) Bitumen-FeOOH
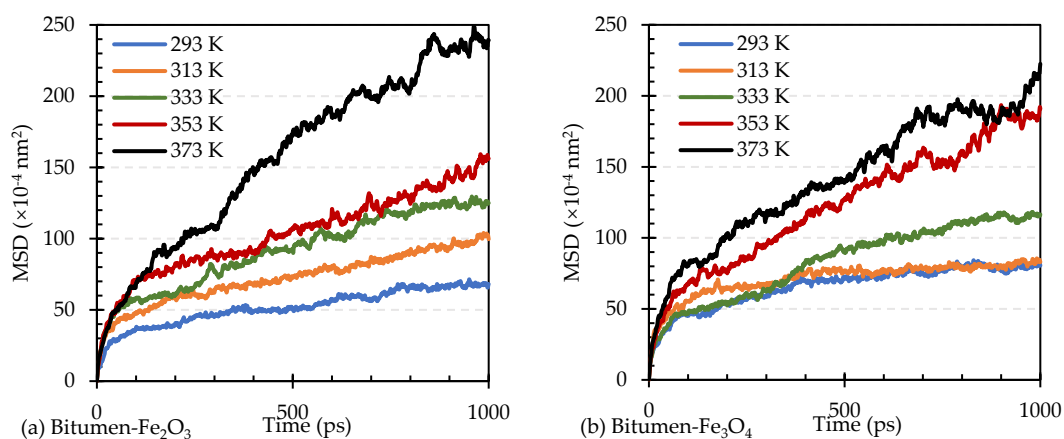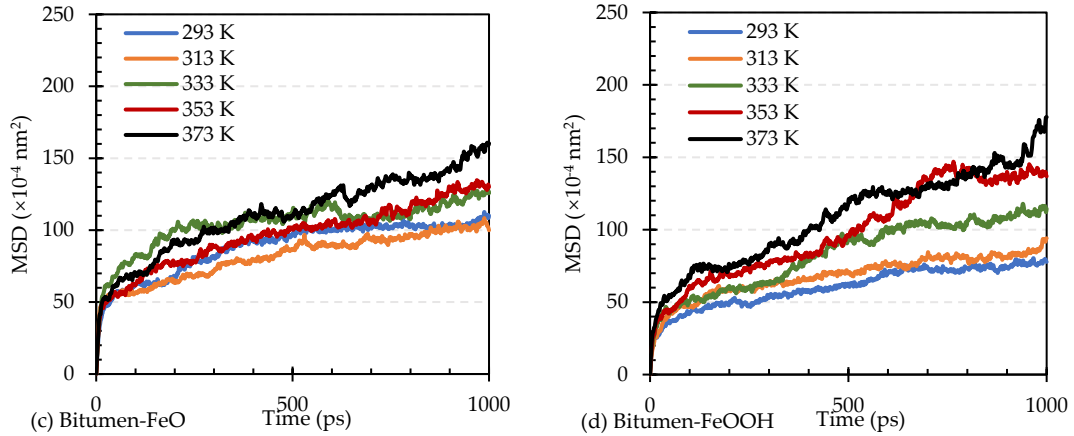
507   Figure 9. The MSD curves of bitumen-corrosion products system at different temperatures.

508

509   It is necessary to determine the simulated time range used for the fitting to calculate the

510   diffusion coefficient. In this research, the MSD curves was transformed into double logarithmic

511   form (log(MSD)-log(t)), then select a section whose slope is as close to 1 as possible to find the

512   diffusion coefficient. Base on Equation (8), and it would be as follows:

$$\log \text{MSD}(t) = \log t + \log (6D) \tag{9}$$

513   Where MSD is mean squared displacement, t is the simulated time and D is diffusion coefficient.

514   By this method, the diffusion coefficients of bitumen-corrosion products system at

515   different temperatures were calculated and shown in Figure 10. A higher slope of MSD curves

516   means a greater diffusivity of molecules. It was found that bitumen molecules on different

517   corrosion products and under different temperature possess distinct diffusion coefficient. The

518   results showed that the diffusivity of bitumen on the surfaces of corrosion products was

519   positively correlated with the van der Waals interaction and electrostatic interaction. The

520   interactions would result in the aggregation of the bitumen on the corrosion products and limit

521   the diffusion of bitumen molecules. Furthermore, it is observed that the interaction between

522   FeOOH and bitumen is weak, but the aggregation degree of bitumen on the surface of FeOOH

523   is not obviously decreased, which demonstrates that electrostatic interaction and van der Waals

524   interaction have different effects on the aggregation degree of bitumen: electrostatic interaction

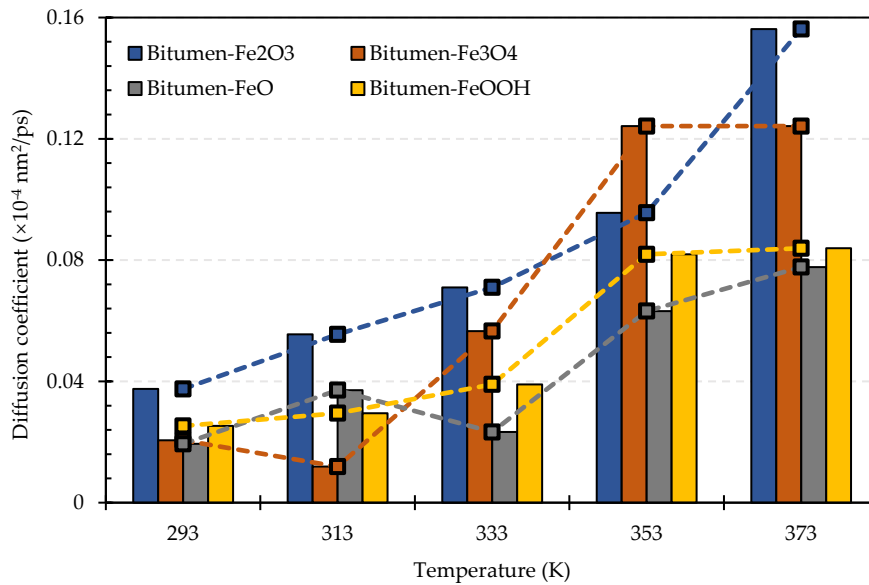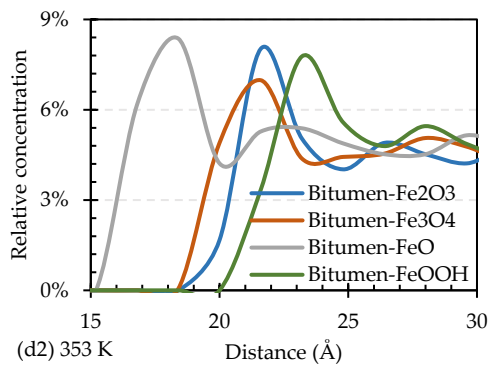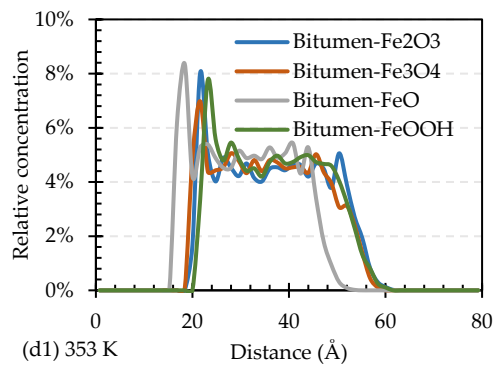525   is more likely to lead to bitumen aggregation on the surface of corrosion products.
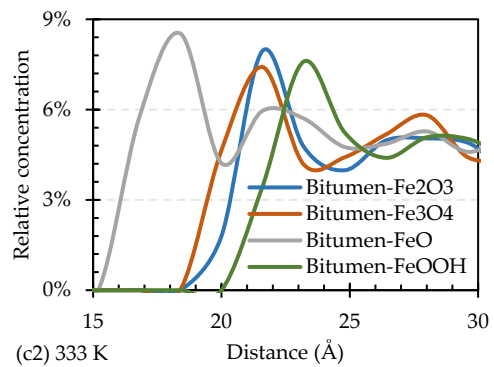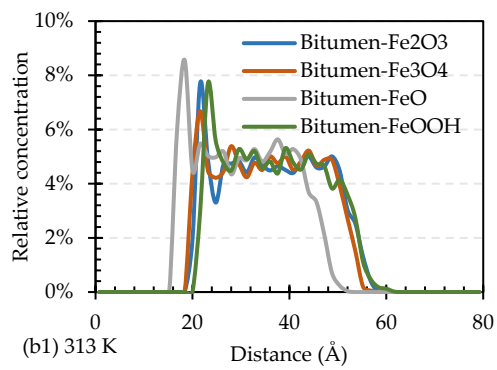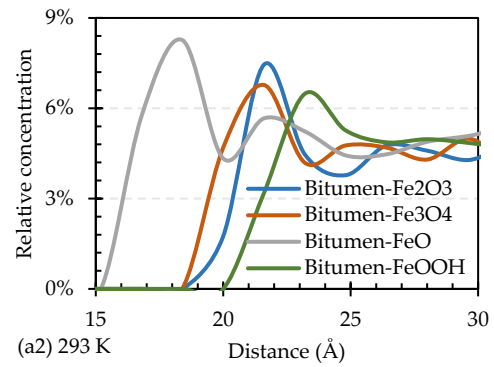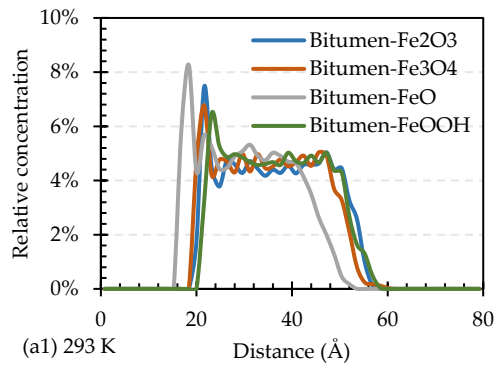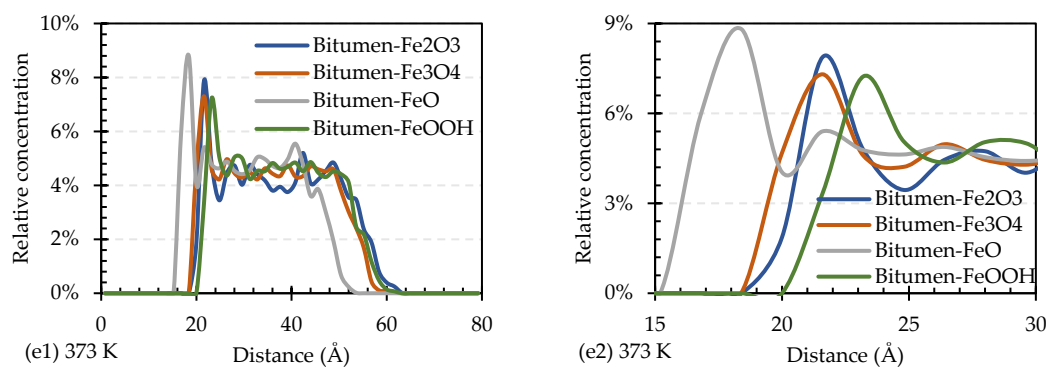
526

Figure 10. The diffusion coefficients of bitumen-corrosion products system at different temperatures.

3.5 Relative concentration of bitumen in bitumen-corrosion products systems

The diffusion coefficient calculated by MSD can only reflect the activity of bitumen molecules in the bitumen-corrosion products system, but it cannot directly evaluate the movement direction of molecules. During the diffusion process, the bitumen would form a layered structure whose concentration would be obviously higher than that of other regions of the bitumen in the system. The intensity of the layered structure can reflect the interaction between bitumen and corrosion products; that is, stronger interaction is responsible for a more prominent layered structure on the products. To understand how the interaction and diffusion was affected by temperature and corrosion product types, the relative distribution concentration of bitumen in the Z-axis direction of the corrosion products was calculated and analyzed. As shown in Figure 11, for the Bitumen-FeO system, relative concentration distributions indicate the two prominent peaks around 18.5 Å and 21.5 Å, while there was only one obvious peak in other systems, indicating that the concentration layers in the Bitumen-FeO system was thicker. The two prominent peaks on the relative concentration of the systems might be related to the double-layer structure on the solid−liquid interface. In a system, the stronger the interaction between bitumen and corrosion products, the closer the peaks are to the products. With increasing distance from the products surface, the oscillations of elative concentration distributions decay and no obvious peak was found.

(a1) 293 K

(a2) 293 K

(b1) 313 K

(b2) 313 K

(c1) 333 K

(c2) 333 K

(d1) 353 K

(d2) 353 K

(e1) 373 K

(e2) 373 K
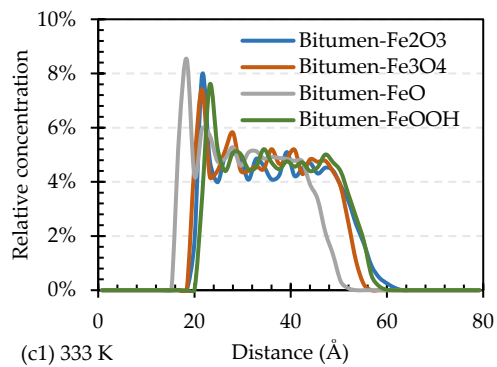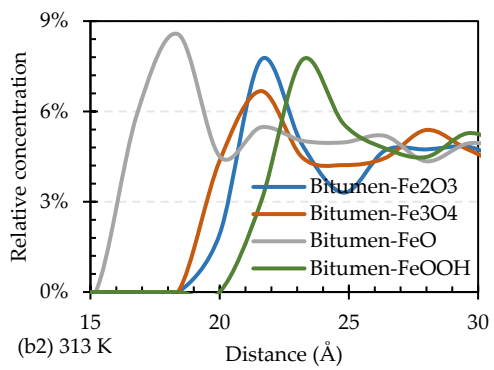
Figure 11. The relative concentration distributions of bitumen on corrosion products at different temperatures: (a1)-(e1) Full-scaled view; and (a2)-(e2) Local-scaled view.

The relative concentration of the first prominent peaks of the bitumen-corrosion products system at different temperature were chosen and shown in the Figure 12. It can be found that the relative concentration was fluctuating with the temperature increasing, but there was no common function to describe the changing. The relative concentration of the first prominent peaks of the bitumen-corrosion products basically showed the regularity of Bitumen-FeO system > Bitumen-Fe$_2$O$_3$ system > Bitumen-FeOOH system > Bitumen-Fe$_3$O$_4$ system, indicating that the aggregation degree of bitumen molecules on the FeO surface was the most severe. It would restrict the diffusion movements of bitumen on the surface and affect adhesion failure mode of the systems. A more severe aggregation degree may indicate a more possible cohesion failure. Moreover, the aggregation degree of bitumen molecules on the FeOOH also indicates that electrostatic interactions are more likely to cause aggregation than van der Waals interactions.
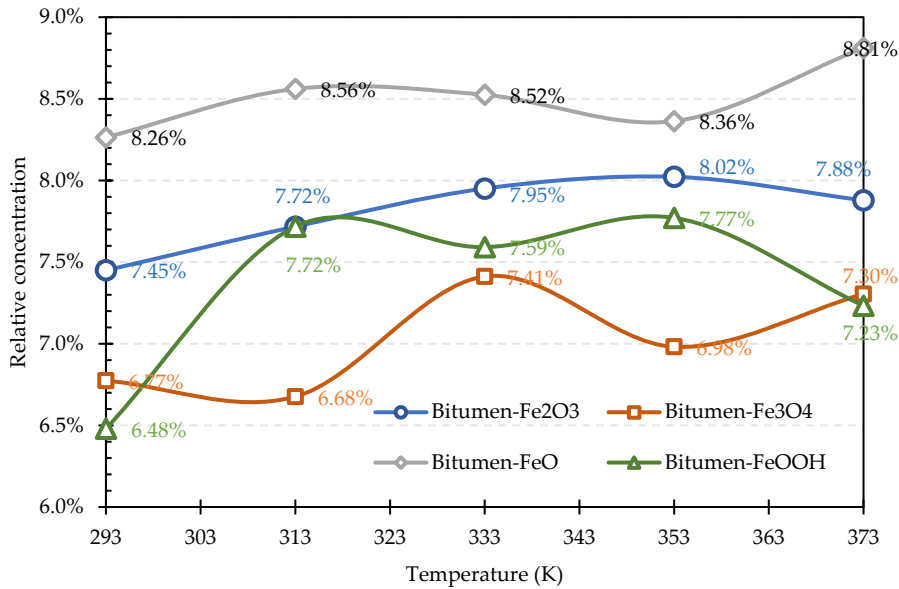
Figure 12. Changes of maximum relative concentration distributions of bitumen-corrosion products systems at different temperatures.

3.6 Interface debonding behaviors between bitumen and corrosion products

Figure 13 shows the debonding process of the bitumen molecules from the surface of corrosion products after the equilibrium. In Figure 13 (a), it can be found that the bitumen molecule model would be stretched and lengthened firstly by the downward movement of the corrosion products. As the corrosion products kept moved, bitumen molecules cannot continue to pull each other, thus the holes would be formed in the model. Finally, more holes were formed, which led to the broken that caused cohesion debonding failure. As opposed to cohesion debonding failure, Figure 13 (b) shows the adhesive debonding where the bitumen molecules were directly and completely debonded with the corrosion products.
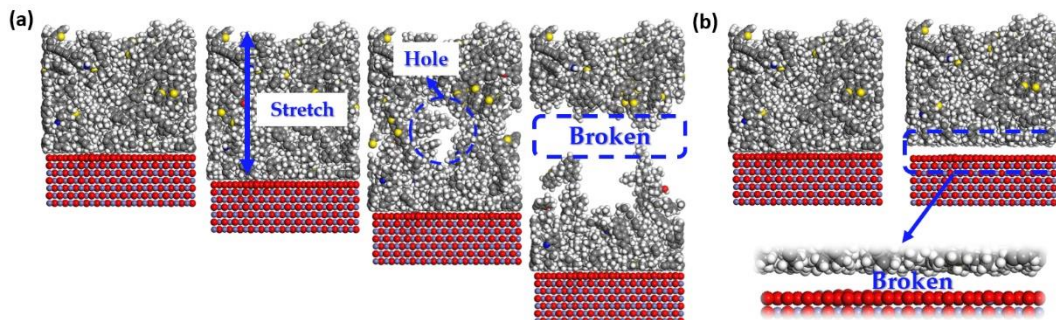

Figure 13. Debonding process at the interface of bitumen and corrosion products: (a) Cohesion debonding; (b) Adhesion debonding

584   Figure 14 represents the residual bitumen molecules on the corrosion products and

585   percentages of cohesive debonding calculated by Equation (4). It can be found that higher

586   pullout velocity had caused less bitumen molecules attached on the corrosion products. When

587   the velocity has reached 0.0405 Å/fs, the CR value were 0% basically, which also means the

588   completely adhesion debonding. The decreasing trend of CR of the bitumen-corrosion

589   products systems were different: CR value of Bitumen-Fe_2O_3 system would gradually decrease

590   until the velocity of 0.0405 Å/fs, CR value of Bitumen-FeO system would keep similar value

591   until the velocity of 0.0405 Å/fs, and CR valaue of Bitumen-Fe_3O_4 system and Bitumen-FeOOH

592   system would keep similar value and decrease from 0.0135 Å/fs. It implied the difference of

593   impacts of speed on different systems: the greatest impact on Bitumen-FeOOH system and the

594   least impact on Bitumen-FeO system. The thickness of bitumen film was also the important

595   factor that influenced on the CR value: it decreased with the thickness thinning, and turning

596   points were 10 Å for Bitumen-Fe_2O_3 system, Bitumen-Fe_3O_4 system and Bitumen-FeO system,

597   and 15 Å for Bitumen-FeOOH system. Furthermore, the results can also validate the interaction

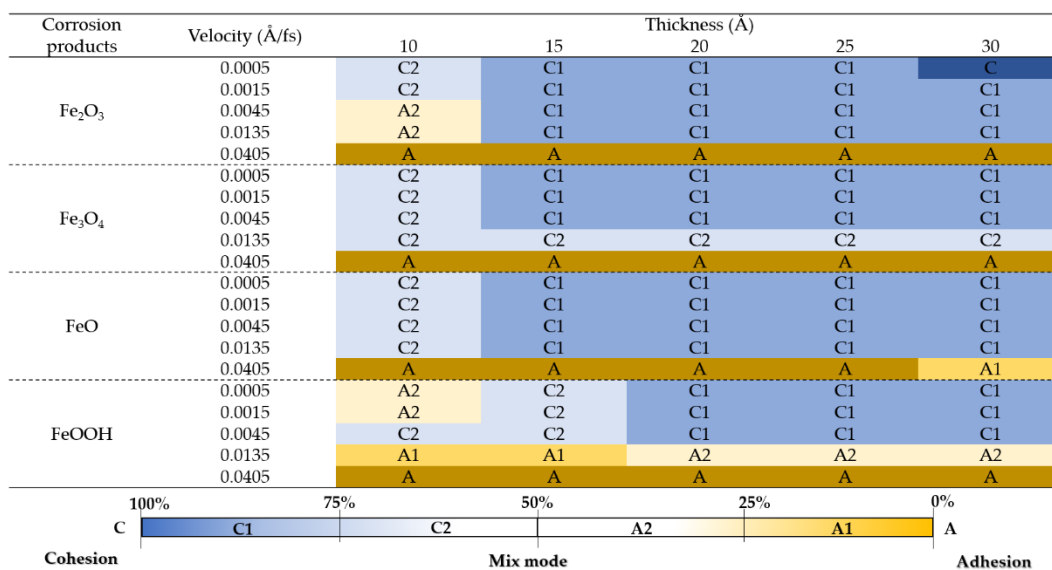598   effect between bitumen and the corrosion products in section 3.3.

599
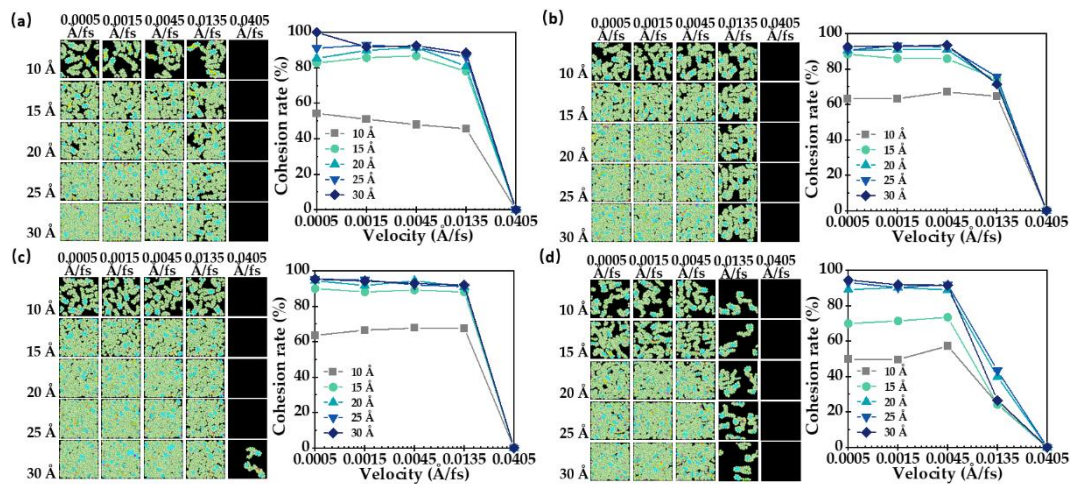
601   Figure 14. The Residual bitumen molecules on the corrosion products and CR value: (a)
602   Bitumen-Fe_2O_3 system; (b) Bitumen-Fe_3O_4 system; (c) Bitumen-FeO system; (d) Bitumen-
603   FeOOH system

604

605   As discussed above, the debonding in bitumen-corrosion products systems was variable

606   under different conditions such as bitumen film thickness and loading rate, which could occur

607   at the bitumen-corrosion products interfaces (complete adhesion debonding) or within the

bitumen (complete cohesion debonding). Actually, the debonding on most occasions should be

a mix mode of cohesion and adhesion. Figure 15 shows the debonding failure type of the

bitumen-corrosion products systems with different velocity and thickness. The failure types

are divided into cohesion, adhesion and mix mode, among which mix mode was divided four

types according to the CR value simply: heavy cohesion (C1), light cohesion (C2), heavy

adhesion (A1) and light adhesion (A2). It can be found that the debonding types would make

a transition from cohesion to adhesion with the increment of velocity and bitumen film

thickness while the smoothness of the systems is different. In particular, it was still light

adhesion mode of Bitumen-FeO system at 30 Å and 0.0405 Å/fs, which shows the strong

interaction between FeO and bitumen. Moreover, the changing of Bitumen-FeOOH system at

10 Å and 0.0045 Å/fs indicated the weak interaction.

Corrosion products	Velocity (Å/fs)	Thickness (Å)				
		10	15	20	25	30
Fe$_2$O$_3$	0.0005	C2	C1	C1	C1	C
	0.0015	C2	C1	C1	C1	C1
	0.0045	A2	C1	C1	C1	C1
	0.0135	A2	C1	C1	C1	C1
	0.0405	A	A	A	A	A
Fe$_3$O$_4$	0.0005	C2	C1	C1	C1	C1
	0.0015	C2	C1	C1	C1	C1
	0.0045	C2	C1	C1	C1	C1
	0.0135	C2	C2	C2	C2	C2
	0.0405	A	A	A	A	A
FeO	0.0005	C2	C1	C1	C1	C1
	0.0015	C2	C1	C1	C1	C1
	0.0045	C2	C1	C1	C1	C1
	0.0135	C2	C1	C1	C1	C1
	0.0405	A	A	A	A	A1
FeOOH	0.0005	A2	C2	C1	C1	C1
	0.0015	A2	C2	C1	C1	C1
	0.0045	C2	C2	C1	C1	C1
	0.0135	A1	A1	A2	A2	A2
	0.0405	A	A	A	A	A

100%　　75%　　50%　　25%　　0%

C　|　C1　|　C2　|　A2　|　A1　|　A

Cohesion　　Mix mode　　Adhesion

Figure 15. Debonding failure type of the bitumen-corrosion products systems with different
velocity and thickness

5　Conclusions

The investigation has been conducted to identify the interfacial characteristics between

corrosion products (Fe$_2$O$_3$, Fe$_3$O$_4$, FeO and FeOOH) and bitumen by molecular dynamics

simulation approach. Based on the results, the primary conclusions are as follows:

(1) The adsorption and adhesion of bitumen was most strongly on the FeO surface and

least strongly on the FeOOH surface. Increased temperature widened the interatomic

gaps in the molecular model of bitumen, which caused the fluctuating decrease in adsorption and adhesion, but it was difficult to be described by an explicit functional relationship with temperature.

(2) The adhesion between bitumen and corrosion products is primarily determined by non-bond interaction energy. In Bitumen-Fe_2O_3 system, Bitumen-Fe_3O_4 system and Bitumen-FeO system, van der Waals interaction was the main contributor, and it was not significantly affected by temperature. In the Bitumen-FeOOH system, both van der Waals and electrostatic interactions played a major role in adhesion, but their contribution decreased with increasing temperature.

(3) The interaction between FeOOH and bitumen is weak, but the aggregation of bitumen on the FeOOH surface is not significantly reduced. Electrostatic and van der Waals interactions contribute differently to the degree of bitumen aggregation, and electrostatic interaction is more likely to cause bitumen aggregation on the surface of corrosion products.

(4) In the debonding process, changes of loading velocity and bitumen film thickness in the debonding process led to the failure transformation between cohesion and adhesion. During the debonding process, cohesion becomes the main failure type in the Bitumen-FeO system due to severe aggregation and strong interaction.

This study exploits molecular dynamics to explore the interfacial behavior between bitumen and corrosion products on steel slag surface. These findings would be contributed to the recycling of steel slag in the pavement engineering. It should be considered to control the corrosion stage and environment, which could adjust the types of corrosion products and increase the thickness of bitumen film. Alternatively, the modification on the surface of corrosion products can also enhance electrostatic interaction to control the failure types.

Author Contributions: **Haiqin Xu**: Conceptualization, Methodology, Data curation, Writing-Original draft, Writing - Review & Editing. **Yingxue Zou**: Methodology, Investigation, Writing - Review & Editing. **Gordon Airey**: Investigation, Writing - Review & Editing. **Haopeng Wang**: Methodology, Investigation, Data curation. **Hanyu Zhang**: Methodology, Investigation, Data curation. **Shaopeng Wu**: Conceptualization, Funding acquisition, Supervision. **Anqi Chen**:

660　　Conceptualization, Methodology, Project administration. **Jun Xie**: Resources, Writing - Review

661　　& Editing. **Yang Liang**: Resources, Writing - Review & Editing.

662

670

671　　**Declaration of Competing Interest**: The authors declare that they have no known competing

672　　financial interests or personal relationships that could have appeared to influence the work

673　　reported in this paper.

674

Reference

676　[1]　Z. Zhao, S. Wu, J. Xie, C. Yang, F. Wang, N. Li, Q. Liu, S. Amirkhanian, Effect of direct
677　　　addition of asphalt rubber pellets on mixing, performance and VOCs of asphalt mixtures,
678　　　Constr.　　Build.　　Mater.　　411　　(2024)　　134494.
679　　　https://doi.org/10.1016/j.conbuildmat.2023.134494.

680　[2]　European Commission. Directorate General for Regional and Urban Policy., Road
681　　　infrastructure in Europe: road length and its impact on road performance., Publications
682　　　Office, LU, 2022. https://data.europa.eu/doi/10.2776/21558 (accessed June 21, 2023).

683　[3]　European Union Road Federation (ERF), Road Asset Management: An ERF Position
684　　　Paper for Maintaining and Improving a Sustainable and Efficient Road Network, (2014).
685　　　https://trid.trb.org/view/1357497 (accessed June 21, 2023).

686　[4]　Ministry of Transport of the People's Republic of China, Statistical Bulletin on the
687　　　Development　　of　　Transportation　　Industry　　in　　2022,　　(2023).
688　　　https://xxgk.mot.gov.cn/2020/jigou/zhghs/202306/t20230615_3847023.html　　(accessed
689　　　June 17, 2023).

690　[5]　C. Yang, S. Wu, J. Xie, S. Amirkhanian, Z. Zhao, H. Xu, F. Wang, L. Zhang, Development
691　　　of blending model for RAP and virgin asphalt in recycled asphalt mixtures via a micron-
692　　　Fe3O4　　tracer,　　J.　　Clean.　　Prod.　　383　　(2023)　　135407.
693　　　https://doi.org/10.1016/j.jclepro.2022.135407.

694　[6]　C. Yang, S. Wu, P. Cui, S. Amirkhanian, Z. Zhao, F. Wang, L. Zhang, M. Wei, X. Zhou, J.
695　　　Xie, Performance characterization and enhancement mechanism of recycled asphalt

696 mixtures involving high RAP content and steel slag, J. Clean. Prod. 336 (2022) 130484.
697 https://doi.org/10.1016/j.jclepro.2022.130484.

698 [7] H. Xu, S. Wu, H. Li, Y. Zhao, Y. Lv, Study on Recycling of Steel Slags Used as Coarse and
699 Fine Aggregates in Induction Healing Asphalt Concretes, MATERIALS 13 (2020).
700 https://doi.org/10.3390/ma13040889.

701 [8] H. Xu, S. Wu, A. Chen, Y. Zou, C. Yang, P. Cui, Study on preparation and characterization
702 of a functional porous ultra-thin friction course (PUFC) with recycled steel slag as
703 aggregate, J. Clean. Prod. 380 (2022) 134983. https://doi.org/10.1016/j.jclepro.2022.134983.

704 [9] P. Cui, S. Wu, Q. Liu, F. Wang, Artificial neural network modeling for predicting surface
705 texture and its attenuation of micro-surfacing containing steel slag aggregates, Constr.
706 Build. Mater. 346 (2022) 128504. https://doi.org/10.1016/j.conbuildmat.2022.128504.

707 [10] P. Cui, S. Wu, Y. Xiao, Q. Liu, F. Wang, Hazardous characteristics and variation in internal
708 structure by hydrodynamic damage of BOF slag-based thin asphalt overlay, J. Hazard.
709 Mater. 412 (2021). https://doi.org/10.1016/j.jhazmat.2021.125344.

710 [11] Z. Chen, S. Wu, Y. Xiao, W. Zeng, M. Yi, J. Wan, Effect of hydration and silicone resin on
711 Basic Oxygen Furnace slag and its asphalt mixture, J. Clean. Prod. 112 (2016) 392–400.
712 https://doi.org/10.1016/j.jclepro.2015.09.041.

713 [12] J. Xie, S. Wu, L. Zhang, Y. Xiao, Q. Liu, C. Yang, S. Nie, Material characterization and
714 performance evaluation of asphalt mixture Incorporating basic oxygen furnace slag (BOF)
715 sludge, Constr. Build. Mater. 147 (2017) 362–370.
716 https://doi.org/10.1016/j.conbuildmat.2017.04.131.

717 [13] P. Cui, S. Wu, Y. Xiao, R. Hu, T. Yang, Environmental performance and functional analysis
718 of chip seals with recycled basic oxygen furnace slag as aggregate, J. Hazard. Mater. 405
719 (2021) 124441. https://doi.org/10.1016/j.jhazmat.2020.124441.

720 [14] A. Shen, C. Zhai, Y. Guo, X. Yang, Mechanism of adhesion property between steel slag
721 aggregate and rubber asphalt, J. Adhes. Sci. Technol. 32 (2018) 2727–2740.
722 https://doi.org/10.1080/01694243.2018.1507505.

723 [15] P. Cui, S. Wu, Y. Xiao, F. Wang, F. Wang, Quantitative evaluation of active based adhesion
724 in Aggregate-Asphalt by digital image analysis, J. Adhes. Sci. Technol. 33 (2019) 1544–
725 1557. https://doi.org/10.1080/01694243.2019.1602912.

726 [16] W. Liu, H. Li, H. Zhu, P. Xu, The interfacial adhesion performance and mechanism of a
727 modified asphalt-steel slag aggregate, Materials 13 (2020).
728 https://doi.org/10.3390/ma13051180.

729 [17] Y. Guo, H. Wu, A. Shen, X. Yang, T. Cui, Study of the long-term water stability of asphalt
730 mixtures containing steel slag aggregate, J. Adhes. Sci. Technol. 34 (2020) 877–902.
731 https://doi.org/10.1080/01694243.2019.1688923.

732 [18] A. Coomarasamy, T.L. Walzak, EFFECTS OF MOISTURE ON SURFACE CHEMISTRY
733 OF STEEL SLAGS AND STEEL SLAG-ASPHALT PAVING MIXES, Transp. Res. Rec.
734 (1995). https://trid.trb.org/view/452574 (accessed October 24, 2023).

735 [19] K.H. JUNG, D.-B. Jang, H.-N. Kim, Evaluation of the Effect of Rust Formation and the
736 Characteristics of Sound Absorption of PSMA Concrete Mixture Using Steel Slag
737 Aggregate, J. Korean Recycl. Constr. Resour. Inst. 9 (2021) 594–601.
738 https://doi.org/10.14190/JRCR.2021.9.4.594.

739 [20] J. Wan, S. Wu, Y. Xiao, M. Fang, W. Song, P. Pan, D. Zhang, Enhanced ice and snow

740   melting efficiency of steel slag based ultra-thin friction courses with steel fiber, J. Clean.
741   Prod. 236 (2019). https://doi.org/10.1016/j.jclepro.2019.117613.

742 [21] J. Wan, S. Wu, Y. Xiao, Z. Chen, D. Zhang, Study on the effective composition of steel slag
743   for asphalt mixture induction heating purpose, Constr. Build. Mater. 178 (2018) 542–550.
744   https://doi.org/10.1016/j.conbuildmat.2018.05.170.

745 [22] K. Suda, S. Misra, K. Motohashi, Corrosion Products of Reinforcing Bars Embedded in
746   Concrete, Corros. Sci. 35 (1993) 1543–1549. https://doi.org/10.1016/0010-938X(93)90382-Q.

747 [23] H. Xu, S. Wu, A. Chen, Y. Zou, Influence of erosion factors (time, depths and environment)
748   on induction heating asphalt concrete and its mechanism, J. Clean. Prod. 363 (2022)
749   132521. https://doi.org/10.1016/j.jclepro.2022.132521.

750 [24] G.S. Duffó, W. Morris, I. Raspini, C. Saragovi, A study of steel rebars embedded in
751   concrete during 65 years, Corros. Sci. 46 (2004) 2143–2157.
752   https://doi.org/10.1016/j.corsci.2004.01.006.

753 [25] LAMMPS Molecular Dynamics Simulator, (n.d.). https://www.lammps.org/ (accessed
754   January 8, 2024).

755 [26] H. A, Z. Yang, R. Hu, Y.-F. Chen, L. Yang, Effect of Solid–Liquid Interactions on Substrate
756   Wettability and Dynamic Spreading of Nanodroplets: A Molecular Dynamics Study, J.
757   Phys. Chem. C 124 (2020) 23260–23269. https://doi.org/10.1021/acs.jpcc.0c07919.

758 [27] M. Benhassine, E. Saiz, A.P. Tomsia, J. De Coninck, Nonreactive wetting kinetics of binary
759   alloys: A molecular dynamics study, Acta Mater. 59 (2011) 1087–1094.
760   https://doi.org/10.1016/j.actamat.2010.10.039.

761 [28] Z. Du, X. Zhu, Molecular Dynamics Simulation to Investigate the Adhesion and Diffusion
762   of Asphalt Binder on Aggregate Surfaces, Transp. Res. Rec. 2673 (2019) 500–512.
763   https://doi.org/10.1177/0361198119837223.

764 [29] J. Xu, B. Ma, W. Mao, W. Si, X. Wang, Review of interfacial adhesion between asphalt and
765   aggregate based on molecular dynamics, Constr. Build. Mater. 362 (2023).
766   https://doi.org/10.1016/j.conbuildmat.2022.129642.

767 [30] H. Xu, Y. Zou, G. Airey, H. Wang, H. Zhang, S. Wu, A. Chen, Wetting of bio-rejuvenator
768   nanodroplets on bitumen: A molecular dynamics investigation, J. Clean. Prod. (2024)
769   141140. https://doi.org/10.1016/j.jclepro.2024.141140.

770 [31] Y. Zou, Y. Gao, A. Chen, S. Wu, Y. Li, H. Xu, H. Wang, Y. Yang, S. Amirkhanian, Adhesion
771   failure mechanism of asphalt-aggregate interface under an extreme saline environment:
772   A molecular dynamics study, Appl. Surf. Sci. 645 (2024) 158851.
773   https://doi.org/10.1016/j.apsusc.2023.158851.

774 [32] Y. Gao, Y. Zhang, F. Gu, T. Xu, H. Wang, Impact of minerals and water on bitumen-
775   mineral adhesion and debonding behaviours using molecular dynamics simulations,
776   Constr.   Build.   Mater.   171   (2018)   214–222.
777   https://doi.org/10.1016/j.conbuildmat.2018.03.136.

778 [33] M. Huang, H. Zhang, Y. Gao, L. Wang, Study of diffusion characteristics of asphalt-
779   aggregate interface with molecular dynamics simulation, Int. J. PAVEMENT Eng. 22 (2021)
780   319–330. https://doi.org/10.1080/10298436.2019.1608991.

781 [34] F. Guo, J. Pei, G. Huang, J. Zhang, A. Falchetto, L. Korkiala-Tanttu, Investigation of the
782   adhesion and debonding behaviors of rubber asphalt and aggregates using molecular
783   dynamics   simulation,   Constr.   Build.   Mater.   371   (2023).

784   https://doi.org/10.1016/j.conbuildmat.2023.130781.

[35] L. Gao, X. Ji, Y. Tan, Z. Wang, Y. Zhang, H. Kong, Molecular dynamics simulation of interfacial adhesion behavior between waterborne epoxy resin emulsified asphalt and aggregate, Compos. Interfaces 30 (2023) 749–770. https://doi.org/10.1080/09276440.2022.2164425.

[36] S. Zhao, H. Zhang, Y. Feng, Y. Hang, Effect of diffusion on interfacial properties of polyurethane-modified asphalt-aggregate using molecular dynamic simulation, Rev. Adv. Mater. Sci. 61 (2022) 778–794. https://doi.org/10.1515/rams-2022-0265.

[37] F. Guo, J. Pei, J. Zhang, R. Li, P. Liu, D. Wang, Study on Adhesion Property and Moisture Effect between SBS Modified Asphalt Binder and Aggregate Using Molecular Dynamics Simulation, MATERIALS 15 (2022). https://doi.org/10.3390/ma15196912.

[38] G. Sun, Z. Niu, J. Zhang, X. Tan, Y. Jing, Z. Chen, Impacts of asphalt and mineral types on interfacial behaviors: A molecular dynamics study, CASE Stud. Constr. Mater. 17 (2022). https://doi.org/10.1016/j.cscm.2022.e01581.

[39] J. Liu, B. Yu, Q. Hong, Molecular dynamics simulation of distribution and adhesion of asphalt components on steel slag, Constr. Build. Mater. 255 (2020). https://doi.org/10.1016/j.conbuildmat.2020.119332.

[40] X. Zhou, G. Zhao, S. Tighe, M. Chen, S. Wu, S. Adhikari, Y. Gao, Quantitative comparison of surface and interface adhesive properties of fine aggregate asphalt mixtures composed of basalt, steel slag, and andesite, Constr. Build. Mater. 246 (2020). https://doi.org/10.1016/j.conbuildmat.2020.118507.

[41] D.D. Li, M.L. Greenfield, Chemical compositions of improved model asphalt systems for molecular simulations, Fuel 115 (2014) 347–356. https://doi.org/10.1016/j.fuel.2013.07.012.

[42] C. Zheng, C. Shan, J. Liu, T. Zhang, X. Yang, D. Lv, Microscopic adhesion properties of asphalt-mineral aggregate interface in cold area based on molecular simulation technology, Constr. Build. Mater. 268 (2021). https://doi.org/10.1016/j.conbuildmat.2020.121151.

[43] N.H. de Leeuw, T.G. Cooper, Surface simulation studies of the hydration of white rust Fe(OH)2, goethite α-FeO(OH) and hematite α-Fe2O3, Geochim. Cosmochim. Acta 71 (2007) 1655–1673. https://doi.org/10.1016/j.gca.2007.01.002.

[44] Wang, Wu, Li, Xu, Xu, Shi, Wang, Microscopic Analysis of Steel Corrosion Products in Seawater and Sea-Sand Concrete, Materials 12 (2019) 3330. https://doi.org/10.3390/ma12203330.

[45] E. Zepeda-Alarcon, H. Nakotte, A.F. Gualtieri, G. King, K. Page, S.C. Vogel, H.-W. Wang, H.-R. Wenk, Magnetic and nuclear structure of goethite (α-FeOOH): a neutron diffraction study, J. Appl. Crystallogr. 47 (2014) 1983–1991. https://doi.org/10.1107/S1600576714022651.

[46] M. Valášková, J. Tokarský, J. Pavlovský, T. Prostějovský, K. Kočí, α-Fe2O3 Nanoparticles/Vermiculite Clay Material: Structural, Optical and Photocatalytic Properties, Materials 12 (2019) 1880. https://doi.org/10.3390/ma12111880.

[47] W.A. Bassett, L.-G. Liu, Experimental determination of the effects of pressure and temperature on the stoichiometry and phase relations of wiistite, (n.d.).

[48] M.H.N. Assadi, J.J. Gutiérrez Moreno, D.A.H. Hanaor, H. Katayama-Yoshida, Exceptionally high saturation magnetisation in Eu-doped magnetite stabilised by spin–

828   orbit interaction, Phys. Chem. Chem. Phys. 23 (n.d.) 20129–20137.
829   https://doi.org/10.1039/D1CP02164H.

830 [49] G. Bahlakeh, M. Ghaffari, M.R. Saeb, B. Ramezanzadeh, F. De Proft, H. Terryn, A Close-
831   up of the Effect of Iron Oxide Type on the Interfacial Interaction between Epoxy and
832   Carbon Steel: Combined Molecular Dynamics Simulations and Quantum Mechanics, J.
833   Phys. Chem. C 120 (2016) 11014–11026. https://doi.org/10.1021/acs.jpcc.6b03133.

834 [50] S.S. Rath, N. Sinha, H. Sahoo, B. Das, B.K. Mishra, Molecular modeling studies of oleate
835   adsorption on iron oxides, Appl. Surf. Sci. 295 (2014) 115–122.
836   https://doi.org/10.1016/j.apsusc.2014.01.014.

837 [51] W.A. Deer, R.A. Howie, J. Zussman, An Introduction to the Rock-Forming Minerals,
838   (2013). https://doi.org/10.1180/DHZ.

839 [52] S. Liu, S. Zhou, A. Peng, Analysis of moisture susceptibility of foamed warm mix asphalt
840   based on cohesion, adhesion, bond strength, and morphology, J. Clean. Prod. 277 (2020)
841   123334. https://doi.org/10.1016/j.jclepro.2020.123334.

842 [53] D.K. Owens, R.C. Wendt, Estimation of the surface free energy of polymers, J. Appl.
843   Polym. Sci. 13 (1969) 1741–1747. https://doi.org/10.1002/app.1969.070130815.

844 [54] Y. Zou, H. Xu, S. Xu, A. Chen, S. Wu, S. Amirkhanian, P. Wan, X. Gao, Investigation of
845   the moisture damage and the erosion depth on asphalt, Constr. Build. Mater. 369 (2023)
846   130503. https://doi.org/10.1016/j.conbuildmat.2023.130503.

847 [55] W. Cui, W. Huang, H. Hassan, X. Cai, K. Wu, Study on the interfacial contact behavior of
848   carbon nanotubes and asphalt binders and adhesion energy of modified asphalt on
849   aggregate surface by using molecular dynamics simulation, Constr. Build. Mater. 316
850   (2022). https://doi.org/10.1016/j.conbuildmat.2021.125849.

851 [56] S.M. Iveson, S. Holt, S. Biggs, Contact angle measurements of iron ore powders, Colloids
852   Surf. Physicochem. Eng. Asp. 166 (2000) 203–214. https://doi.org/10.1016/S0927-
853   7757(99)00455-0.

854